Large-Strain Piezoelectric Actuators Using Controlled Structural Buckling

by

Devin Michael Neal

B.S., Mechanical Engineering, Massachusetts Institute of Technology, 2007

Submitted to the Department of Mechanical Engineering in partial fulfillment of the requirements for the degree of

Master of Science in Mechanical Engineering

at the

MASSACHUSETTS INSTITUTE OF TECHNOLOGY

September 2009

Author .....
Department of Mechanical Engineering
August 21, 2009

Certified by .....
H. Harry Asada
Ford Professor of Mechanical Engineering
Thesis Supervisor

Accepted by .....
David E. Hardt
Chairman, Department Committee on Graduate Students
Department of Mechanical Engineering

Large-Strain Piezoelectric Actuators Using Controlled Structural Buckling

by

Devin Michael Neal

Submitted to the Department of Mechanical Engineering
on August 21, 2009, in partial fulfillment of the
requirements for the degree of
Master of Science in Mechanical Engineering

Abstract

Buckling is a highly nonlinear and singular phenomenon in thin beams, and is usually an undesired characteristic that must be prevented from occurring in engineered systems. Buckling, however, can be a useful mechanism for gaining extremely large displacement amplification, since a infinitesimal displacement in the axial direction of the beam may lead to a large deflection in the middle of the beam. This thesis presents a novel large-strain piezoelectric actuator exploiting the buckling of a structure with imbedded piezoelectric stack actuators. The realization of this buckling actuator began by rethinking the paradigm of where PZT stacks are placed in traditional flexure-based displacement amplification mechanisms. Although the free displacement of a PZT stack is only 0.1% of the stack length, the buckling mechanism can produce a large bipolar displacement that is approximately 150 times larger than the original PZT displacement. Furthermore, the structural buckling produces a pronounced nonlinearity in output impedance; the effective stiffness viewed from the output port varies as a function of output displacement, which can be a useful property for those applications where actuator stiffness needs to vary. Buckling is controlled with phased activation of the input units and either 1) a strategically placed redirecting stiffness or 2) multiple buckling units working in parallel.

Thesis Supervisor: H. Harry Asada
Title: Ford Professor of Mechanical Engineering

Acknowledgments

First, I must thank the sources of funding, without which this research would not have been possible. I thank Sumitomo Heavy Industries for the generous financial support towards this research and other research efforts in the d'Arbeloff laboratory at MIT. I also thank the MIT Presidential Scholarship program for the generous fellowship that permitted me to find the research position best suited to my skills and interests at the beginning of my graduate studies.

I would like to thank two members of the D'Arbeloff who contributed to this research directly. I thank Tom Secord for providing me with his knowledge of the field, and his meticulously engineered and crafted custom hardware. I thank Professor Asada for being my advisor and friend. I thank him for catering this research project to my strengths. I have learned immensely from our brainstorming sessions, as well as his teachings on technical writing and presentation techniques. He has made it clear to me through his actions, that his most valued contribution to engineering is his students.

I would like to thank Georgette Neal, my mom, most of all. She has shown me what it means to work hard, to earn what I receive, and the importance of contributing to society. Her work ethic and desire for perfection inspire me daily.

Contents

List of Figures

List of Tables

Chapter 1

Introduction

Piezoelectric actuators possess many desirable properties for linear actuators. They have very high typical efficiency, power density, and maximum frequency. Shape memory alloy (SMA) actuators have similar maximum stiffness values, but achieve typical efficiencies of 0.01-0.02, whereas high-strain piezoelectric actuators achieve efficiencies of 0.90-0.99 [1]. Moreover, SMA actuators are more difficult to control due to thermal issues from operation. Piezoelectric actuators have long life expectancies as opposed to conducting polymers such as polypyrrole despite their high potential strain of 12% [2]. Conducting polymers must also maintain a wet environment, thus limiting actuators' work environment. Dielectric elastomers are capable of very high strain up to 215%, but are undesirable due to a high voltage requirement (4-6 kV for centimeter scale applications) [3]. Additionally, piezoelectric ceramic actuators have been implemented in MEMS strain amplification mechanisms, thus increasing the potential application space [4].

The greatest shortcoming of piezoelectric actuators is the limited strain they produce. Unamplified strains are on the order of 0.1%, well below a reasonable goal of about 10% achievable by skeletal muscle. Piezoelectric strain amplification has been a subject of research for the past few decades. A number of different methods have been developed including internally leveraged (bi-morph bending cantilevers and uni-morph bowing actuators), externally leveraged (lever arm, hydraulic, and flextensional actuators), and frequency leveraged actuators (inchworm actuators) [5].

Internally leveraged actuators exhibit substantial displacement but with significantly decreased force due to the strain energy absorbed in bending and low stiffness. Frequency leveraged actuators require significant additional hardware, limiting performance per overall density and increasing fabrication complexity.

Flextensional strain amplification mechanisms have been in development for over forty years. They were originally designed for acoustic purposes, but have since been designed to maximize output deflection and force [6]. These actuators designed for displacement include the Moonie [7] and the Cymbal [8]. These designs are modular and have been stacked serially to increase net displacement [9]. Serial flextensional actuators have also been used as input actuators to second-layer flextensional actuators, thus increasing net displacement and strain. Strains of 21% are possible using this multilayer "nested rhombus" method [10]. Although the strain is significant and similar in magnitude to achievable strain in skeletal muscle, the output force of multilayer flextensional actuators is not sufficient for many applications. To increase this output force, a new flextensional concept has been developed. The first contribution of this work is similar to the rhombus like mechanisms, and generate similar displacement. However, the characteristics are unique two ways. First, the displacement amplification factor decreases with displacement providing greater force while actively displaced. Second, the actuator actively elongates, rather than actively shortens as with past flextensional actuators. Actively elongating is particularly valuable if within a "nested rhombus" as it prevents unwanted buckling and increases output force.

Additionally, this thesis presents an alternative to existing methods by exploiting a pronounced nonlinearity of structural mechanics: buckling. This nonlinear and singular phenomenon can produce an order-of-magnitude larger effective strain amplification in a single stage. The nonlinearities arising in mechanisms and structural mechanics have typically been thought of as parasitic properties. Strain amplification mechanisms have been designed to keep the output an approximately linear function of input actuator force and displacement. Two novel methods of controlling buckling are presented through design, simulation, and prototypes.

Buckling violates this linear input-output requirement. The amplification gain is not merely large, but it varies significantly within the movable range. Accordingly, mechanical advantage and stiffness at the output port may vary depending on the displacement. These nonlinearities can be useful if their properties are matched with the load characteristics. For example, biologically inspired robots need varying actuator stiffness, where the velocity-force relationship must vary along a gait cycle or a flapping cycle [11], [12]. Nonlinear transmissions, such as the buckling mechanism addressed in this thesis, will open up new possibilities in developing unique machines.

Chapter 2

Design Concept

2.1 Significant Performance Differences over Previous Designs

The presented design is very similar to previous designs like the Moonie and other flextensional mechanisms having an overall rhombus shape. The basic concept of previous designs has been to incorporate an expandable material between two corners of a rhombus-like structure as diagramed in Fig. 2-1. The stiff rhombus sides are connected with compliant joints. The corresponding output axis is along the other two corners of the rhombus-like structure. As the material oriented perpendicular to the output axis expands, the output corners of the rhombus-like structure move closer to each other.

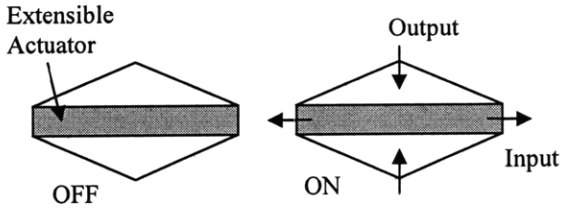

Figure 2-1: Traditional rhombus-shaped external strain amplification mechanism.

The new concept places the input actuators as the sides of a rhombus-like structure with a stiff element connecting the non-output corners of the rhombus, as shown in

Fig. 2-2. The important features of the presented new design are analogous to the previous external mechanism designs. The ideally stiff rhombus sides of previous designs are similar to the extensible material rhombus sides. The extensible material between the non-output corners of the rhombus in previous designs corresponds to the ideally stiff material between those corners in the current design.

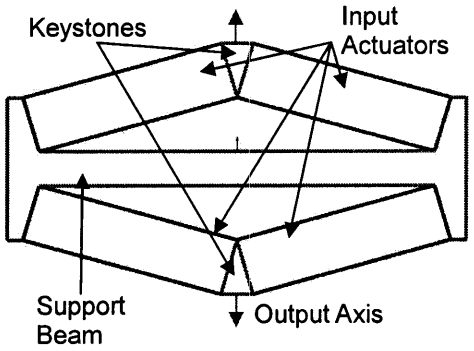

Figure 2-2: Presented amplification concept configuration.

Two significant differences arise when placing the input actuators at the sides of the rhombus rather than between the non-output corners. First, the direction of output motion relative to input motion does not change as it did in previous designs. In this design, as the input actuators extend, the output axis of the mechanism also extends.

This is of great significance for multi-layered actuators where buckling is likely to occur due to beam compression. Using the output of a rhombus mechanism as the input of yet another rhombus mechanism has been shown to exponentially increase strain amplification. Such designs have achieved greater than 20% strain using two layers with piezoelectric actuators [10]. When more common flextensional mechanisms with internally located input actuators are used as both layers in a dual-layer mechanism, the active output direction is extension, as shown in Fig. 2-3. The input of the second layer (output of first layer) is a shortening motion. When a shortening motion is used as the input for a traditional flextensional mechanism, the output activation motion is extensional. When this extensional motion is used to force a load, the ideally stiff rhombus sides of the second layer are put in compression, and are thus likely to buckle, severely decreasing the achievable load force of the overall

mechanism.

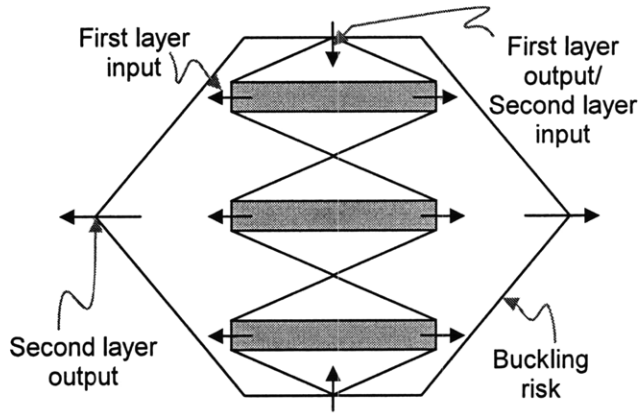

Figure 2-3: Dual-layer mechanism with internally placed input actuators.

Using the presented design, with externally placed input actuators as the first layer and the more traditional design as the second layer in a dual-layer mechanism, the device actively shortens. Such a mechanism is diagrammed in Fig. 2-4. Due to the active shortening, an external load would place the second layer ideally stiff rhombus sides in tension, thus eliminating the potential for buckling. The only beam elements in the entire mechanism in compression are the input actuators, and they are necessarily in compression due to the nature of ceramic piezoelectric stacks.

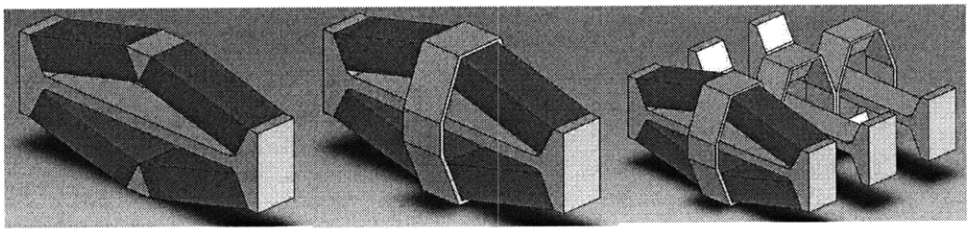

Figure 2-4: Dual-layer actively shortening displacement amplification assembly.

The second significant difference of externally placed input actuators is that as the input actuators extend, the angle each rhombus side makes with the support beam, θ, increases. As will be shown in the next section, the output force goes approximately linearly with this angle, θ. Combining the fact that piezoelectric crystal output force decreases with displacement with the fact that output force increases as the angle,

θ, increases provides an opportunity to manipulate the net force-displacement curve of the overall mechanism in interesting ways. For example, the force-displacement curve could be made to be relatively constant for small displacements, the blocking force (zero displacement) could be made to equal the force at a specified nonzero displacement, and/or the mechanism could be made to be bistable upon activation. Actuators with bistable force curves, depicted in Fig. 2-6, have potential to provide benefits in energy efficiency and controllability.

2.2 Kinematic Analysis of Strain Amplification

Consider the case where the mechanism is actuated by actuators of zero width. The upper left quarter of this scenario is illustrated in Fig. 2-5. The length L is the unactuated, unforced length of the actuator. As the material is actuated, the non-moving end is constrained to rotate in place, while the moving end is constrained to move along the output axis. As the actuator length increases from its rest length, L, to $L + \Delta L$, the dimension along the output axis increases from y to $y + \Delta y$, and the angle between the actuator axis and a surface perpendicular to the output axis, Δ, increases to $\theta + \Delta\theta$.

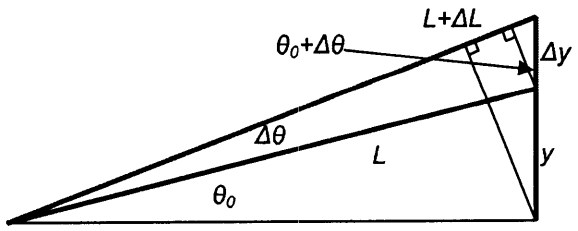

Figure 2-5: Quarter view of rhombus structure with externally placed input actuators.

The length the input actuator extends, ΔL, is given by its strain as $\Delta L = L\varepsilon$. The initial output dimension, y, is a function of the initial angle, θ_0, and length, L, as $y = L\sin(\theta_0)$. As displacement occurs, the change in output length, Δy, changes as a function of the actuator's change in length, ΔL, the initial angle, θ_0, and the

change in angle, $\Delta\theta$. For small values of θ_0 and $\Delta\theta$, the expression for Δy reduces to,

$$\Delta y = \frac{L\left[1 - \cos\left(\Delta\theta\right)\right] + \Delta L}{\sin\left(\theta_0 + \Delta\theta\right)} \approx \frac{\Delta L}{\theta_0 + \Delta\theta}. \tag{2.1}$$

Assuming values of $\Delta\theta$ that are small compared to θ_0, combining this output displacement, Δy, with the initial length of the mechanism in the output direction, y, a first order expression for output strain is given as,

$$\varepsilon_{out} = \frac{\Delta y}{y} = \frac{L\varepsilon}{\sin\left(\theta_0 + \Delta\theta\right)} \cdot \frac{1}{L\sin\left(\theta_0\right)} \approx \frac{\varepsilon}{\theta_0^2}, \tag{2.2}$$

where ε_{out} is the output strain, and ε is the strain of the input actuator. Thus, the strain amplification goes approximately as the square of the initial angle, θ_0. For example, an initial angle of 10 degrees yields an ideal strain amplification of approximately 3300%.

The output force is given by,

$$F_o = 2F_i \sin\left(\theta_0 + \Delta\theta\right) \approx 2F_i\left(\theta_0 + \Delta\theta\right), \tag{2.3}$$

where F_o is the output force, and F_i is the input force of each actuator. Keep in mind that two input actuators influence each output "keystone." An approximation for the individual piezoelectric stack actuator force displacement relation is,

$$F_i \approx F_{bi} - \frac{F_{bi}}{\varepsilon_{\max}}\varepsilon, \tag{2.4}$$

where F_{bi} is the input actuator blocking force, and ε_{max} is the input actuator free strain.

An exact expression for $\Delta\theta$ is,

$$\Delta\theta = \cos^{-1}\left(\frac{\cos\left(\theta_0\right)}{1+\varepsilon}\right) - \theta_0. \tag{2.5}$$

2.3 Utility of Introduced Nonlinearities

Using Eq. 2.1, 2.3, 2.4, and 2.5, the effects of θ increasing with active displacement on the output force-displacement curve can be observed. As depicted in Figure 6, the output force as a function of output motion approaches a negative parabola for small values of θ_0. The function is the quotient of two linear functions, one with positive slope, and the other with negative slope. The negative sloped curve is the force-strain relationship of the input actuator given in Eq. 2.4. The positive sloped curve is from an approximate output force, F_o, to output displacement, Δy, relationship described in the following paragraph.

Another geometric expression for output displacement is,

$$\Delta y = \frac{L \sin(\Delta\theta)}{\cos(\theta_0 + \Delta\theta)} \approx L\Delta\theta. \tag{2.6}$$

Equation 2.6 shows a linear relationship between Δy and $\Delta\theta$, while Eq. 2.3 shows a linear relationship between F_o and $\Delta\theta$ for a constant F_i and small values of θ_0 relative to $\Delta\theta$. Thus, the relationship between F_o and Δy is approximately linear for small values of θ_0. Equation 2.3 also shows that the positive slope becomes less significant as θ_0 increases; Thus, the force-displacement function becomes more linear as seen in the curve for $\theta_0 = 2.5°$ in Fig. 2-6.

The advantage of having the potential for either a linear or more parabolic shape is that it lends versatility to the actuator. Three significant output force-displacement relationships diagrammed in Fig. 2-6 are 1) an approximate linear negative slope ($\theta_0 = 2.5°$), 2) an approximate slope of zero resulting in approximately constant force over a significant range of displacement ($\theta_0 = 1°$), and 3) a slope that changes from positive to negative with displacement resulting in a bistable output ($\theta_0 = 0.1°$). The designer is thus granted the option to choose. A negative linear slope may be desirable for applications requiring a constant stiffness. A constant force would be desirable if a constant load is to be maneuvered over a large displacement range. The bistable configuration offers high stiffness and high displacement for loads under a specific magnitude, similar to the discrete actuation of stepper motors. Bistable

configurations could be precisely controlled with discrete/binary control, decreasing the need for sensing and feedback control of individual actuator units.

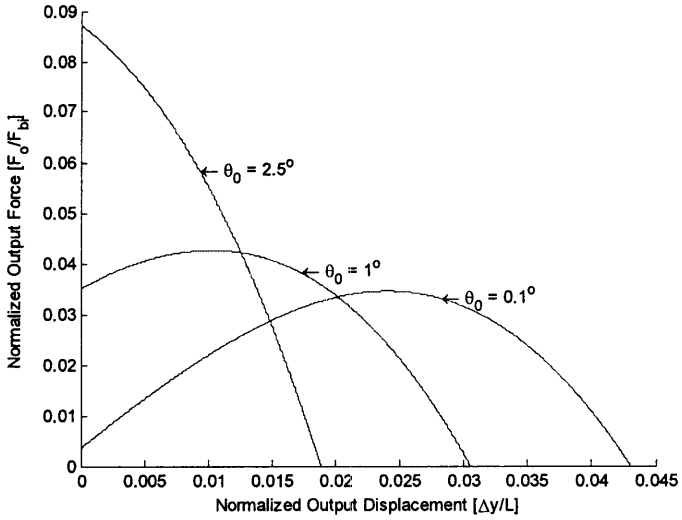

Figure 2-6: Effects of an increasing θ on output assuming a maximum input actuator strain of 0.1%.

2.4 Structural Compliance/Stiffness Model

The output force and displacement performance characteristics are somewhat hindered by structural compliance/stiffness values of the mechanism. Five important stiffness values combine to form the lumped parameter model shown in Fig. 2-7. The stiffness k_{pzt} is the inherent stiffness of the input actuator. The stiffness k_B is the net stiffness of structural elements in series with the input actuator. This includes the tensile stiffness of the support beam, k_b, the shear stiffness of the support beam material in shear, k_{sh}, and the compressive stiffnesses of the interface/rotation joint between the support beam and the input actuator, k_{jc}. The stiffness k_J is the resulting translational stiffness from the rotational stiffness of the rotation joint that allows the angle, θ, to change. Significant additional compliance in k_B would result from the beam buckling of the rhombus sides in traditional amplification mechanisms using actively shortening input actuators. No beams of the presented mechanism are placed in compression; Thus, buckling is not a problem and buckling stiffness does

not contribute to k_B.

The output blocking force, F_{bo}, and output free displacement, Δy_{max}, in terms of individual input actuator blocking force, F_{bi}, stiffness values, k_{pzt}, k_J, k_B, and amplification ratio, a, are,

$$F_{bo} = \frac{k_B}{a\left(k_B + k_{pzt}\right)} 2F_{bi}, \tag{2.7}$$

and

$$\Delta y_{\max} = a\frac{k_B}{k_{pzt}\left(k_B + k_J\right) + k_J k_B} 2F_{bi}. \tag{2.8}$$

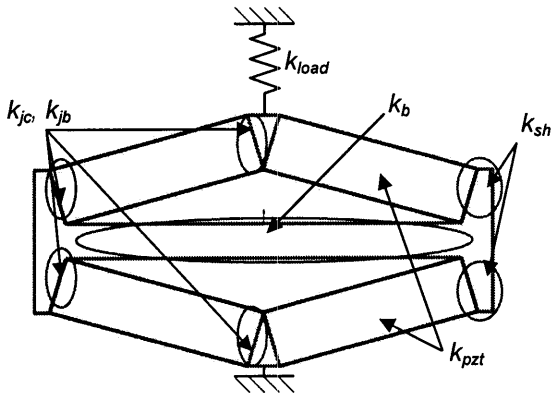

(a) Important Structural Stiffness Locations of Externally Placed Input Actuator Rhombus Mechanism

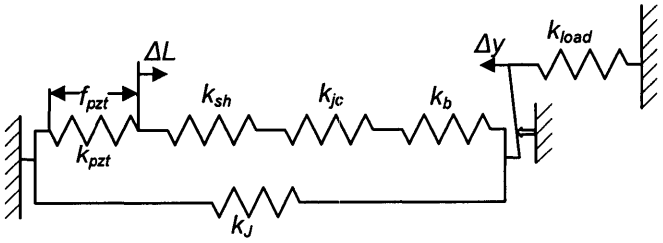

(b) Parameterized Stiffness Model

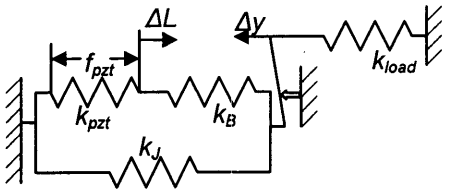

(c) Lumped Parameter Model

Figure 2-7: Lumped parameter model of single strain amplification layer.

The overall design goal of the mechanism is to provide output strain on the order of

10% while maintaining high power density. A value that goes approximately linearly with power density is total energy output by volume per stroke. This energy density may be used as a design parameter to maximize in selecting dimension values involved in critical stiffness elements. Assuming a linear output force-displacement relationship (i.e. not parabolic or bistable), the energy density per stroke by volume goes as $F_{bo}\Delta y_{max}/V$, where V is the volume. By using density by volume rather than by mass, designs are penalized for having essentially wasted gaps of space.

Chapter 3

Implementation of Externally Placed Actuator Design

3.1 Initial Implementation and Evaluation

A number of initial prototypes were designed and tested. To minimize the effects of variation associated with individual PZT stacks and manufacturing techniques, early prototypes consisted of one half of the whole rhombus-like structure. These consisted of two individual PZT stacks forcing a single keystone, braced between a single stiff beam.

To test each prototype, the mechanism is situated as seen in Fig. 3-1. One side of the mechanism is placed against a grounded surface. The other side interfaces to a force transducer through a thin strip of shim stock. The other side of the force transducer then interfaces with a micrometer screw gauge that is rigidly grounded. The purpose of the shim stock is to provide a surface to measure with a laser micrometer. The laser micrometer is rigidly grounded and measures the displacement of the shim and, thereby, the output displacement of the mechanism.

To measure the blocking force, the micrometer is used to apply just enough preload to the entire experimental assembly such that force changes linearly with displacement. This ensures that all interfaces are sufficiently coupled. Next, the laser micrometer makes an initial reading. Then, the appropriate voltage is applied to the

PZT stacks, and the screw gauge is adjusted until the reading on the laser micrometer is restored to the initial value. The force transducer then provides a reading of the force needed to essentially keep the output of the mechanism from being displaced. This is the blocking force.

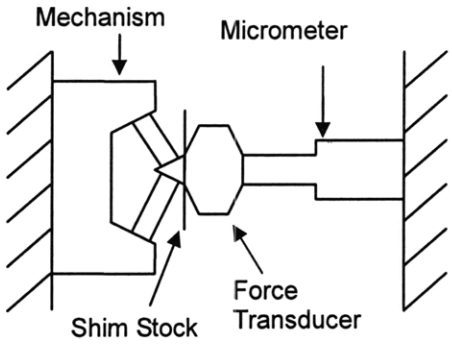

Figure 3-1: Experimental setup for measuring prototype output force.

The final iteration of this prototype phase, shown in Fig. 3-2, produces a blocking force in excess of what we are currently able to measure, 217 N. Subtracting a necessary preload of 50 N, the minimum blocking force is 167 N. This iteration used an initial angle of 20 degrees. Using first-order kinematic relations, the ideal expected output force for 2 PZT stacks with 800 N of blocking force each is approximately 560 N. The ratio of actual blocking force to ideal blocking force is therefore 30% at a minimum. However, the blocking force was significantly greater than what was measured.

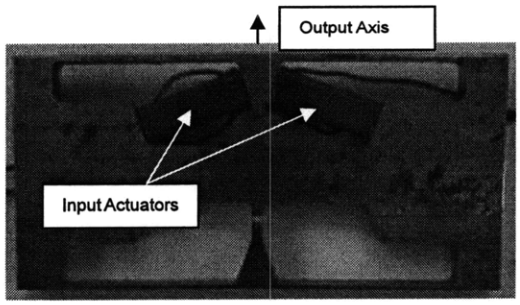

Figure 3-2: Final iteration of initial prototype phase.

The displacement amplification of this prototype is also close to ideal. The measured free displacement is 40 μm, and Eq. 2.1 estimates a displacement of 43 μm.

That represents a ratio of measured to ideal displacement of 93%.

The implementation of multiple prototypes and evaluation of their performance provided significant insight on the causes of the suboptimal force and displacement performance at smaller angles. The roots of these causes are critical design considerations.

3.2 Critical Design Considerations

3.2.1 Shearing Force on PZT Stack

Shear force on PZT stacks has been a concern since the initial concept of this mechanism was developed. If we assume that the PZT stack rotates about two edges, then the stack must experience two forces equal in magnitude at these edges pointing toward each other, as depicted in Fig. 3-3.

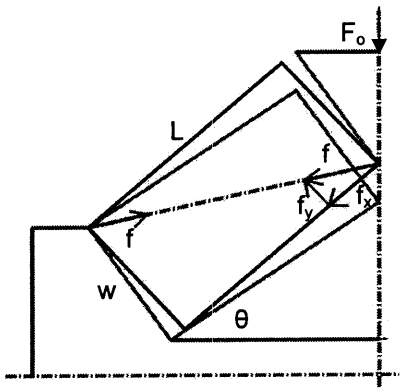

Figure 3-3: Axial and shear forces resulting from rotation about actuator edges.

Due to the width of the PZT stack, there must be some shear force perpendicular to the output axis of the stack. Assuming the displacement is small, the width-to-length ratio of the PZT stack is small, and a small initial angle, θ_0, geometric relations yield,

$$\begin{aligned} f_y &= f_x \tan^{-1}\left(\tfrac{w}{L}\right) \approx f_x \cdot \tfrac{w}{L}, \\ F_O &= 2 \cdot f_x \sin(\theta) \approx 2 \cdot f_y \tfrac{w}{L}\theta. \end{aligned} \quad , \tag{3.1}$$

where f_y is the shear force, f_x is the stack output force, w is the stack width, L is the stack length, and F_o is the output force. Keep in mind that 2 stacks are generating force. This relationship sets a limit on the output force given a maximum allowable shear stress. This result also makes clear that a small width-to-length ratio of the input actuator is desirable.

3.2.2 Compression through a Critical Angle

An important issue, witnessed first hand through prototype experiments, concerns limitations of the PZT stack dimensions on the initial angle. For an initial angle in excess of what will be referred to as a critical angle, θ_c, the PZT stacks will be forced to initially compress as the actuator extends, and go through a point of maximum compression mid stroke. This problem is diagramed in Fig. 3-5.

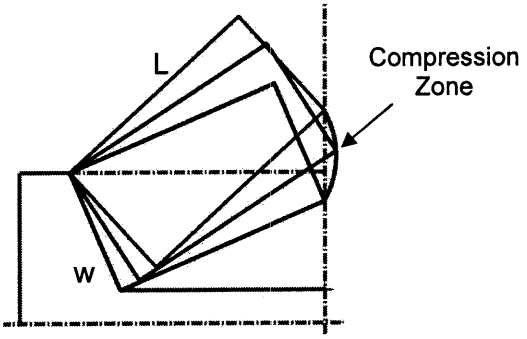

Figure 3-4: Compressive stress resulting from actuation.

The mechanism will only be capable of generating significant displacement if it can overcome the maximum force generated mid-stroke. This will generate excess shear on the PZT stack, and create a bistable actuator. Although bistable performance may be desirable, using ceramic crystals as the necessary compliance is not desirable as it is likely to reduce the lifetime of individual input actuators. This critical angle, θ_c, as a function of the PZT stacks' width, w, and length, L, is,

$$\theta_c = \tan^{-1}(w/L) \approx w/L. \tag{3.2}$$

Again, performance is limited by the ratio of actuator width to length.

3.2.3 Stress Concentration on PZT Stack Actuators

An issue that must be addressed is the stress concentration created by the PZT stack rotating about edges. As can be seen in Fig. 3-5, upon rotation, a force greater than the input force of the stack, f_x, is exerted at each edge of rotation. This problem could easily be mitigated with the addition of end caps on each end of each PZT stack, as shown in Fig. 3-5. The end caps would serve to redistribute stress across a broader face of the PZT stack. The interfacing sides of the end caps may also be beveled or rounded to change the point of rotation. The material can also be selected for hardness as well as durability. They would decrease the effective width-to-length ratio of the input actuator, thus resulting in a decreased critical angle, θ_c, and a lower shear-to-output force ratio. The major drawbacks of including end caps are lower effective input actuator strains and the introduction of additional compliant elements in series with the input actuator.

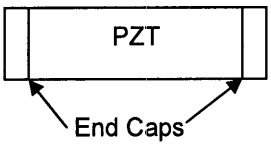

Figure 3-5: Input actuator endcaps.

3.3 Addressing Design Considerations

The goal of the mechanism is to efficiently amplify actuator output strain, and Eq. 2.2 shows that a small initial angle, θ_0, is required to achieve high strain. Initial prototypes were angle limited because of the problems of the critical angle, θ_c, due to mid-stroke compression. Figure 3-6 shows three concepts for keystones that could allow for shallower angle and greater strain amplification. Each incorporates the concept of stack end caps to reduce force concentrations. Each centers the point of rotation along the centerline of the input actuator axes to reduce undesirable shear stress imposed on input actuators. Furthermore, each eliminates the need to worry about critical compression angles.

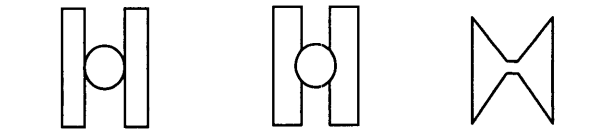

Figure 3-6: Improved keystone concepts.

Figure 3-6(a) shows PZT stack end caps that roll without slipping along a central cylinder. Rolling conserves near-zero joint stiffness. However, rolling also produces contact stress that will add compliance in series with the input actuators. Figure 3-6(b) shows PZT stack end caps that slide around a central cylinder. The larger surface area will result in less additional compliance than the rolling joint. However, the friction forces will severely hinder performance for small angles. Figure 3-6(c) shows PZT stack end caps joined together via a flexure. The flexure provides significant stiffness without negative effects from friction. However, the flexure adds unwanted stiffness parallel to the input actuator, thus contributing to k_J, as shown in Fig. 2-7.

3.4 Flexure Pivot-Based Design

Flexure elements are widely used as rotational bearings in PZT strain amplification mechanisms, both on a macro level and MEMS level [4], [13]. The drawback to using flexure bearings in strain amplification is degradation in performance related to three separate stiffness related factors. As noted above, the bending stiffness contributes to the stiffness, k_J, in parallel with the input actuator; Thus, the greater the joint stiffness, k_J, the weaker the performance of the mechanism. Additionally, the compressive stiffness of the joints contributes compliance to the overall beam stiffness, k_B, in series with the input actuator. The third potentially performance-reducing factor is buckling that could occur if the flexure joint is put under compression. Buckling compliance reduces the output stiffness, k_B, thus further reducing the overall output performance.

3.5 Flexure Pivot-Based Prototype Evaluation

Producing a significant blocking force with an uncompromised strain of order 10% was the ultimate goal in producing the latest prototype actuator. The AE0505D18 PZT stack actuators were selected as the input actuators. Their dimensions are specified as 6.5 mm by 6.5 mm by 18 mm, with a blocking force of 800 N and free displacement of 15 μm at 100 V [14].

With the specifications of the input actuators and a selection of the joint type, the actuator prototype was optimally designed for maximum output energy per stroke by volume. The dimensions of the flexural joints and support beams contributed directly to volume, and the stiffnesses of the lumped parameter model described by static mechanics Eq. 2.7 and Eq. 2.8. Equations 2.1, 2.3, and 2.5 are the kinematic equations that define the output force and displacement as functions of the geometric values θ_0, and $\Delta\theta$. The dimensions of the input actuator, yield stress of the selected material, and manufacturing dimension limitations provide constraints. High yield stress 8620 alloy steel was the selected material. The selected manufacturing process was wire EDM using a 0.010 inch (0.254 mm) diameter wire.

Figure 3-7 shows the first layer optimally designed prototype. The performance of this design was determined by measuring the output blocking force and output free displacement. The values are summarized in Table 3.1.

Table 3.1: Prototype performance.

	Input Actuator	First Layer	Second Layer
Blocking Force	800 N	126 N	19.9 N
Free Displacement	15 μm	329 μm	1.51 mm
Free Strain	0.083%	1.37%	3.73%

A second layer was optimally designed using a similar approach to the design of the first layer. Furthermore, the second layer was manufactured and experimentally evaluated. Fig. 3-8(a) shows the second layer prototype and Fig. 3-8(b) shows the fully assembled actuator. The second layer is more traditionally rhombus-like in structure; one for which the angle, θ, actively decreases, and the output axis actively

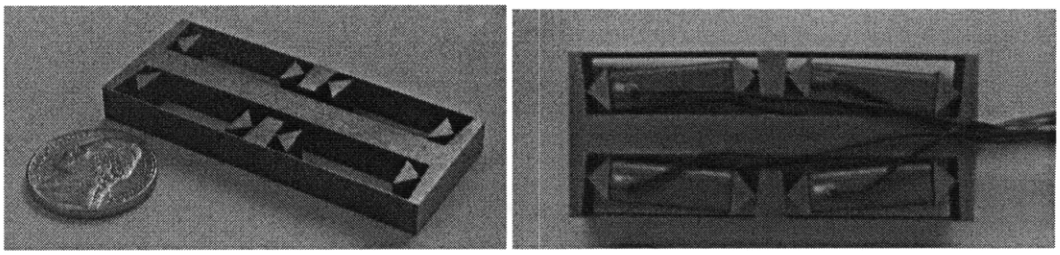

a) First Layer b) Assembled First Layer

Figure 3-7: Prototype single layer actuator.

contracts for an expanding input actuator. A significant constraint on the design was due to the manufacturing process. The thickness of the flexure elements was selected to ensure a durable prototype that would not distort or break during manufacturing, and application. This value was more than twice the optimal thickness value given by corresponding kinematic and static mechanics equations, and contributed significantly to the joint stiffness, k_J. From Eq. (8), one can see that increasing k_J decreases the free displacement of the structure. However, from Eq. (7), one can see that the magnitude of k_J has no influence on the output blocking force. The experimental results are summarized in Table 3.1. The blocking force is a substantial 19.9 N.

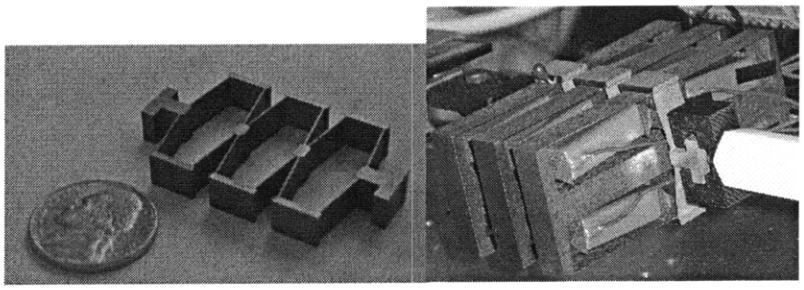

a) Second Layer b) Second Layer Full Assembly

Figure 3-8: Dual layer actuator prototype.

The second layer is capable of manipulating a substantial preload through most of it's free displacement stroke. This prototype was intended for use as the fine positioning actuator is a large assembly. The load will vary between 0 and 5 pounds (22.2 N) of constant force. The mechanism has demonstrated its ability to manipulate such preloads, by moving a 24.2 N constant load over a range of 1.44 mm.

Chapter 4

Buckling Configuration

4.1 Buckling Design Concept

Figure 4-1 shows the schematic of a nonlinear, large-strain PZT actuator, consisting of a pair of PZT stacks and a monolithic structure. The monolithic structure holds the PZT stacks between a keystone output node and the end supports placed at both sides. The end supports are connected to the main body ideally through rotational joints.

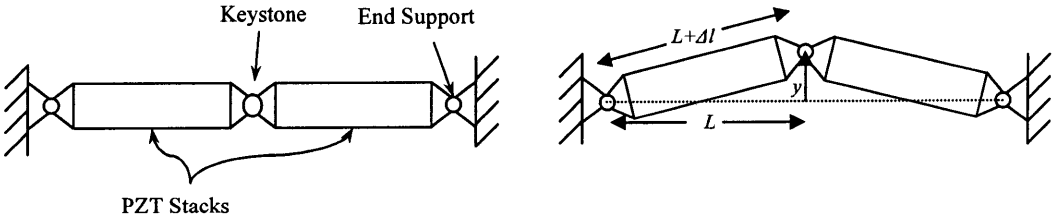

Figure 4-1: Buckling kinematics.

As the PZT stacks are activated, they tend to elongate, generating a large stress along the longitudinal direction. When the two PZT stacks are completely aligned, the longitudinal forces cancel out, creating an unstable equilibrium. With any disturbance, the two PZT stacks tend to rotate, i.e. "buckle." Let Δl be the elongation of each PZT stack and Δy be the vertical displacement of the keystone output node. The displacement amplification ratio, $G = \frac{\Delta y}{\Delta l}$, tends to infinity as y approaches 0. Since $y^2 = (L + \Delta l)^2 - L^2$, G can be computed as,

$$G \cong \frac{L}{y} \to \infty, \text{ as } y \to 0 \tag{4.1}$$

This is a type of kinematic singularity. Even for a finite PZT displacement, the amplification gain, G, is significantly large.

Although this buckling mechanism can provide extremely large strain amplification, buckling is in general an unpredictable, erratic phenomenon, which is difficult to control. We do not know which direction the output node will move, upward or downward. It is also not feasible to quasi-statically bring the output keystone from one side to the other across the middle point. Once it goes upwards, it tends to stay there, and vice versa. This is in a sense "mono-polar" activation where the stroke of the output keystone is half of the total possible displacement. Therefore, it is desirable to both control the buckling direction, and have the capability to pass through the singularity point to the other side once buckling has occurred.

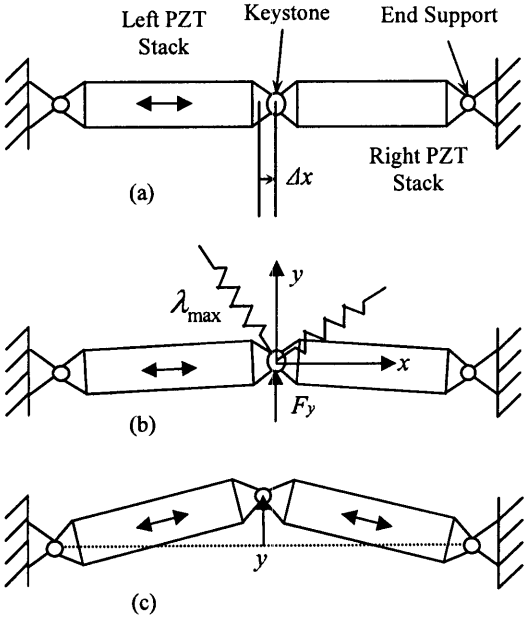

Figure 4-2: Force in the y direction generated by displacement in the x direction.

4.2 Redirecting Principle Axes of the Stiffness Matrix to Control Buckling Direction

To fully control the buckling direction and thereby attain a bipolar, full stroke range of activation, this thesis presents a novel technique called "lateral activation." Instead of activating both PZT stacks at the same time, we activate one PZT stack first followed by the other stack. Suppose that the left PZT stack, for example, is first activated. This creates a sideways displacement of the output node, Δx, in the positive x direction, as shown in Fig. 4-2(a). As mentioned above the output keystone is suspended elastically in both x and y directions. The trick is that this two-dimensional stiffness is tuned in such a way that, in response to sideways displacement Δx, a force along the y-axis is created. As shown in Fig. 4-2(b), the induced force F_y tends to push the output keystone in the positive y direction. Once it is pushed upwards, the output keystone is accelerated in the positive y direction due to the unstable nature of the equilibrium. As the other PZT stack (right PZT) is activated together with the first (left PZT), the y directional displacement increases further. This results in a large displacement in the upward direction. See Fig. 4-2(c). If we activate the right PZT stack first, followed by the left PZT, then the output keystone will move downwards creating a negative y displacement. Therefore, we can fully control the direction of buckling by simply selecting the switching sequence between the two PZT stacks.

The key to this controlled buckling via lateral activation is the two-dimensional stiffness with which the output keystone is suspended. Let $\mathbf{K}$ be a 2 x 2 matrix relating the restoring force vector $(F_x \quad F_y)^T$ acting on the keystone to the displacement vector of the keystone $(\Delta x \quad \Delta y)^T$:

$$\begin{pmatrix} F_x \\ F_y \end{pmatrix} = -\mathbf{K} \begin{pmatrix} \Delta x \\ \Delta y \end{pmatrix}, \quad \mathbf{K} = \begin{pmatrix} K_{xx} & K_{xy} \\ K_{xy} & K_{yy} \end{pmatrix} \tag{4.2}$$

It is clear that, if the off-diagonal element is less than zero, $K_{xy} < 0$, the y directional force becomes positive $F_y > 0$ in response to positive Δx, and vice versa. Note that $\mathbf{K}$ is a positive definite, symmetric matrix with two principal axes associated

with two positive eigenvalues, $\lambda_{\max} > \lambda_{\min} > 0$. It is important to note that the two eigenvalues must be distinct and that the directions of the principal axes are not aligned with the x and y axes, the longitudinal and transverse directions of the dual PZT stacks. The condition for positive off-diagonal stiffness, $K_{xy} < 0$, is achieved by directing the first principal axis associated with $\lambda_{\max}$ to have negative slope. See Fig. 4-2(b). This condition can be realized with many structure designs.

Figure 4-3 shows a schematic time chart of activating the dual PZT stacks. As the left PZT is activated prior to the right PZT, the output displacement goes upwards. In the following sequence the order is reversed, creating a downward output displacement. Thus, the actuator is bipolar and the full stroke is double the single sided displacement. It should be noted that each PZT is turned on and off twice as the output displacement makes one full cycle of movement. This means that the PZT activation frequency is twice that of the frequency of the output movement. For those applications where cyclic motion must be generated, i.e. flapping and running, the bipolar dual PZT activation scheme described above results in an equivalent gear reduction of 1:2. Since the bandwidth of PZT stacks is too high to exploit efficiently for most robotics applications, this effective gear reduction contributes to improving power density.

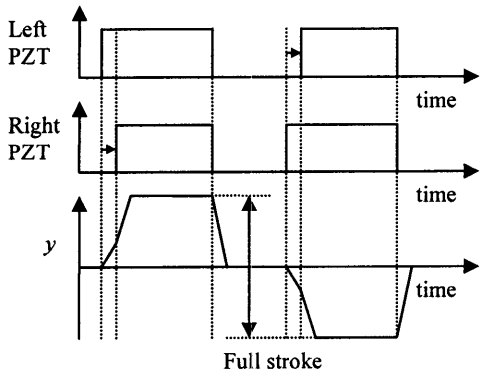

Figure 4-3: Time chart of bipolar activation scheme.

Figure 4-4 shows a simplified model of the entire mechanism. The PZT stacks, along with the flexure supports in series, are represented as springs with stiffness k_p. The rotational stiffness of the flexure supports are assumed small compared to the

redirecting stiffness, k_s. The PZT stacks are modeled as linear. The activation level of each stack varies its unforced length. Each stack's unforced length variation level, u_l for the left stack and u_r for the right, ranges from 0 to the free displacement of the PZT stack, typically about 0.1% of the total length of the stack.

The placement of the grounding point of the redirecting spring (x_s, y_s) is very important because this spring is intended to provide a high output axis force from lateral displacement, K_{xy}, while inhibiting motion in the output axis, y, as little as possible. If the ratio of x_s to y_s is too small, the spring will impede motion in the output axis more than is necessary. If the ratio of x_s to y_s is too great, the spring will not provide enough force along the output axis to lateral displacements, i.e. $|K_{xy}|$ will not be large enough. Ideally, $|K_{xy}|$ need only be finite, but in application, practical disturbances along the output axis and tolerances along the x-axis necessitate a specific minimum value.

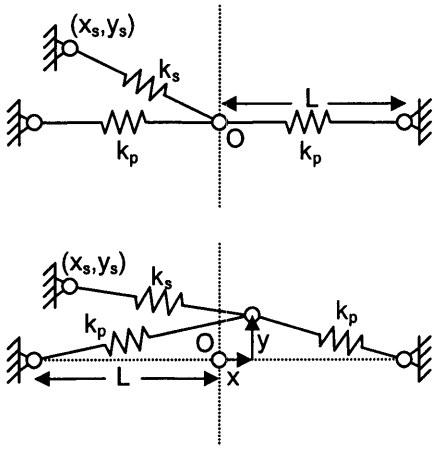

Figure 4-4: Simplified static model of PZT buckling mechanism.

To find a good value to use we start with the simple kinematic model in Fig. 4-5. With no forces, the free displacement of one PZT stack causes the output node to rotate about the grounded node of the other PZT stack. Motion of the output node lies approximately along the cord OA. The slope of this cord is $\Delta y/\Delta x \approx L/y$. Stiffness along this direction causes degradation of performance. In order to prevent generating force against this motion, the redirecting spring should be aligned close to perpendicular to this cord. The instantaneous slope of the trajectory changes

from infinity to $\approx L/y$ as the motion progresses. Therefore, when positioning the grounding point of the redirecting spring, the ratio of x_s to y_s should be between 0 and y/L.

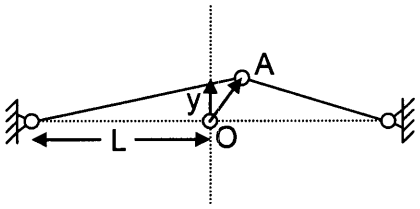

Figure 4-5: Kinematic model with no off-orthogonal stiffness.

Without force, displacement, or K_{xy} specifications to design to, about $y/(2L)$ is a good ratio to use to achieve high force, high displacement, and a high $|K_{xy}|$ value at zero output displacement.

4.3 Redirected Stiffness Simulation

For the simulation, I use PZT stacks with length, L, of 18 mm, a maximum free displacement, u_{max}, of 15 μm, and stiffness of 800 N/15 μm = 5.3e7 N/m. The ratio of x_s to y_s is $y/(2L)$ where y is the pre-computed free displacement in the output direction. The grounding point of the redirecting spring is in the first quadrant and its stiffness, k_s, is chosen to be equal to the stiffness of the PZT stacks. This provides a good balance of providing a high $|K_{xy}|$ vs. increasing K_{yy} and degrading performance.

The potential energy within each modeled spring is a function of the positions in the lateral axis, x, output axis, y, and the left and right unforced length variation levels, u_l and u_r respectively. The total potential energy, U, is given by,

$$\begin{aligned}
U_s &= \tfrac{1}{2}k_s\left(\sqrt{(x_s-x)^2+(y_s-y)^2}-\sqrt{{x_s}^2+{y_s}^2}\right)^2,\\
U_L &= \tfrac{1}{2}k_p\left(\sqrt{(L+x)^2+y^2}-(L+u_L)\right)^2,\\
U_R &= \tfrac{1}{2}k_p\left(\sqrt{(L-x)^2+y^2}-(L+u_R)\right)^2,\\
U(x,y,u_L,u_R) &= U_s+U_L+U_R.
\end{aligned} \tag{4.3}$$

The negative derivative of the potential energy function with respect to either x or y is the force along that axis. Points in the potential energy field where any movement along either axis results in additional potential energy, or "valleys," represent unforced, steady state positions of the actuator. Fig. 4-6 shows the contour plots of the energy function for different values of unforced length variation. Each plot has at least one valley. The left hand side of each plot pair is the function with no redirecting stiffness ($k_s = 0$), where as the right hand side is the function with positive stiffness ($k_s > 0$). A number of interesting points can be made based on these plots.

First, notice that in Fig. 4-6(a), both plots have a valley centered at the origin, and both plots are symmetric about two orthogonal axes. The plot with $k_s = 0$ is symmetric about the x-axis and the y-axis. These axes are parallel to the eigenvectors of the stiffness matrix, $\mathbf{K}$, of Eq. 4.3. Thus, the right energy plot shows that the eigenvectors of $\mathbf{K}$ are not orthogonal to the x and y axes at $y = 0$.

Next, consider the two plot pairs with only one PZT input actuator active (Fig. 4-6(b) and (c)). The plots with $k_s = 0$ are symmetric around the x-axis indicating that $dU/dy = 0$ for $y = 0$. This means there is no force along the y direction, and the actuator prefers neither direction over the other. Alternatively, the plots with $k_s > 0$ are not symmetric about any constant y value axis. In fact, the slope at any point in the function points towards the single valley on one side of the x-axis. This means that, at any point, the output node will feel a force in the direction of the valley on the desired side of the singularity position. From Fig. 4-6, if only the left PZT is active, the actuator will tend towards a negative y value, and if only the right PZT is active, the actuator will tend towards a positive y value. Note that for other values of k_s and ratios of x_s to y_s, two valleys may occur, one on each side of the $y = 0$ axis; however, the value of dU/dy is still in the preferred direction for $y = 0$, i.e. from the singularity position, the actuator displacement direction is still controlled.

Finally, observe the contour plots for the case where both PZT stacks are active, Fig. 4-6(d). Both plots have two valleys, and both plots have $dU/dy = 0$ for $y = 0$ as can be seen from the fact that the contour lines are perpendicular to the x-axis for $y = 0$. Both plots show that if the position is either above or below the x-axis,

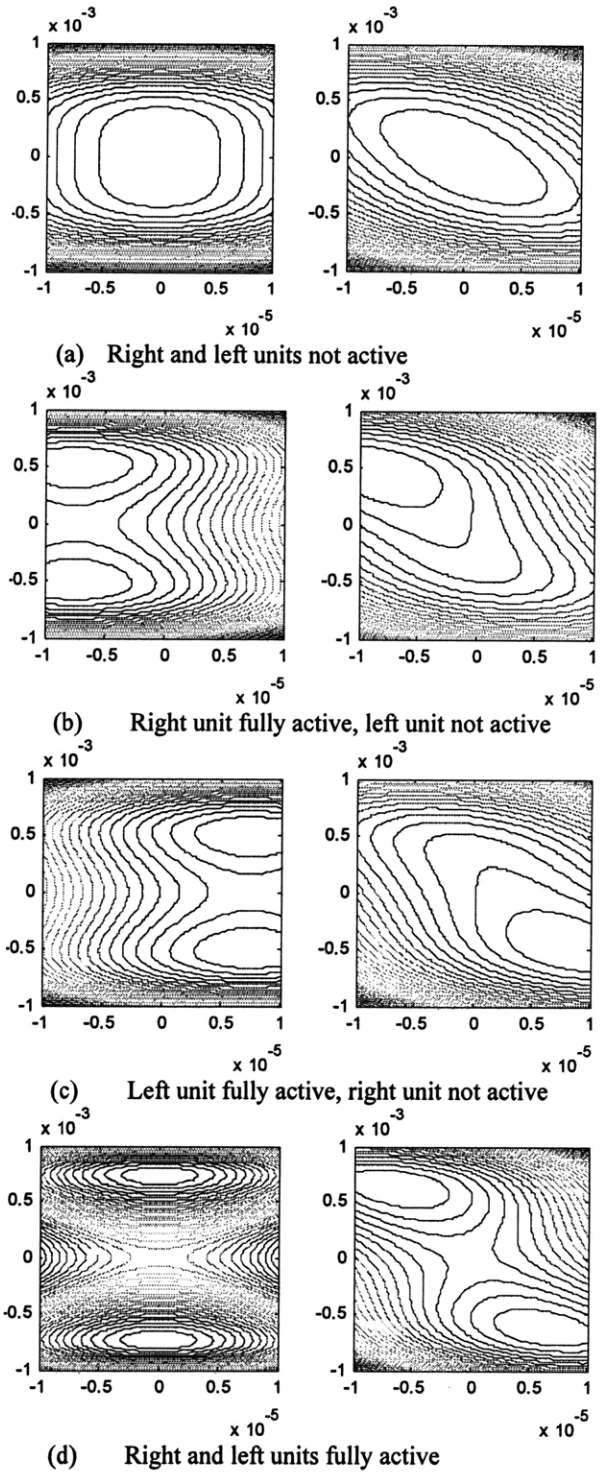

Figure 4-6: Contour plots of potential energy as a function of output axis position, y, and lateral position, x. The left column corresponds to simulation results with no redirecting stiffness, whereas the right column corresponds to results with a redirecting stiffness. Axes units are in meters.

the output node will be forced to the valley respectively above or below the x-axis. However, for $k_s > 0$, both PZT stacks would not be simultaneously fully active unless $y \neq 0$. The magnitude of the y displacement in the valleys for $k_s > 0$ is less than 20% less than the magnitude for $k_s = 0$. This means that the free displacement is degraded by less than 20% for motion in one direction. However, both directions can be controlled with $k_s > 0$, thus the total displacement is overall more than 60% greater.

4.4 Dynamic Motion Analysis

One of the primary utilities of passing through the singularity point is to achieve significant displacement amplification from a single amplification step while maintaining a high frequency output. If we assume that a mass, m, is manipulated by the actuator and that m is significantly greater than the rotational inertia of the PZT stacks, the kinetic energy in the system is simply $m\dot{y}^2/2$. If we activate the two PZT stacks simultaneously, assume motion in the lateral direction is negligible, and neglect effects from the redirecting stiffness or rest angles for multi-unit actuator, the potential energy function simplifies to,

$$k_p\Big(\sqrt{L^2+y^2}-(L+u)\Big)^2, \tag{4.4}$$

where u is the unforced length variation for both units. Using Lagrange's equation, the equation of motion becomes,

$$2k_p\frac{\Big(\sqrt{L^2+y^2}-(L+u)\Big)\,y}{\sqrt{L^2+y^2}}+m\ddot{y}=0 \tag{4.5}$$

Though the stiffness changes throughout the stroke, a dominant resonant frequency exists, for a finite value of u, at which the displacement is maximized. Neglecting perturbing factors, this frequency is the same on either side of the singularity. Simulation of Eq. 4.5 shows that square wave activation at this frequency generates larger displacements than those achieved from quasi-static displacement.

4.5 Stiffness Analysis of Buckling Concept

The force of the actuator in the direction of positive displacement of the output node may be found by computing $-dU/dy$. Similarly, the stiffness along the output direction is computed as d^2U/dy^2. Consider a single buckling actuator. When both PZT stacks are activated, the stiffness as a function of output displacement is highly nonlinear. The force and stiffness curves with $x = 0$ for the simple buckling actuator are shown in Fig. 4-7.

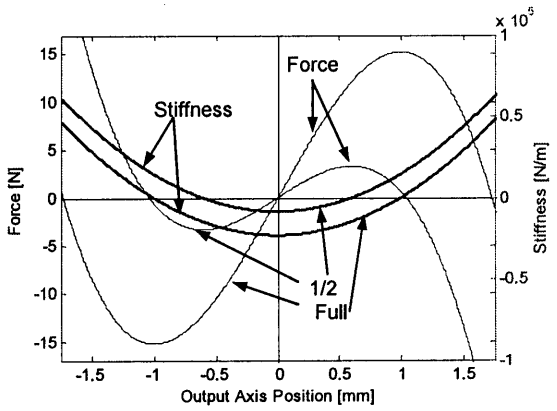

Figure 4-7: Stiffness and force of the actuator output node along the output axis as a function of output node position for two activation levels: 1/2, and full activation.

There are a few important features to note about a single buckling actuator that can be seen in Fig. 4-7. First, there is significant displacement amplification of the actuator. The displacement in a single direction is greater than 1.5 mm at full activation, i.e. 150 V. Compared to the maximum free displacement of the PZT stack (15 μm), this buckling actuator produces 100 times larger displacement. Second, there are nonlinear force-displacement characteristics. The maximum force is generated not at the zero-displacement ($y = 0$), but at a middle stroke. In turn no force is generated at the singular point at $y = 0$. Thirdly, the stiffness varries. Near the singular point, the stiffness is zero or negative, whereas it increases sharply as displacements get larger in either direction.

The second feature above significantly differs from the inherent PZT stack properties and the properties of conventional strain amplification mechanisms, where the

peak force, i.e. blocking force, is created when no displacement is made. The output force decreases monotonically, as displacement increases. In contrast, the buckling actuator produces its peak force mid-stroke. This nonlinear force-displacement relationship is useful, as we exploit later in designing multi-unit actuators.

Furthermore, the buckling actuator exhibits a unique stiffness characteristic; stiffness becomes zero, or even negative with non-zero activation level, in the vicinity of the singular point. This is useful for arranging multiple units in an array. When one unit moves in the vicinity of the singular point, it is effectively "disengaged" from other units, so that it may not be a "load" for the other units producing forces. Using these features of buckling actuators, we have designed multi-unit actuators with minimal mechanical conflict for achieving large bipolar displacement and improved force-displacement characteristics described in the next chapter.

4.6 Buckling Actuator Prototypes

4.6.1 Uncontrolled Buckling Implementation

A proof-of-concept prototype was designed, built, and tested in order to demonstrate the static and dynamic performance of passing through the singularity point. The prototype is shown in Fig. 4-8. The PZT stacks in this prototype are 40 mm long, have a free displacement of 42 μm, and a blocking force of 850 N.

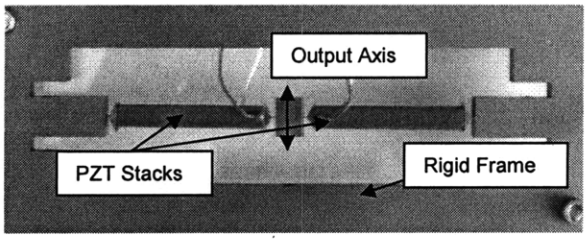

Figure 4-8: Prototype that passes through singularity point capable of 2.37 mm of displacement at 53 Hz, and measured force of 10.8 N.

Through experimentation, we found that the natural frequency of using the actuator on one side of the singularity is in fact approximately equal to the peak-to-peak

natural frequency of using the actuator on both sides alternatively.

To achieve this frequency traveling on both sides, the PZT stacks must be activated at twice this frequency. From the singularity point, they must be activated to reach the maximum displacement in one direction, then deactivated to return, then re-activated to reach the maximum displacement in the other direction, and deactivated once more to return to the original position. This completes one cycle of the actuator. Thus, the PZT stacks cycle on and off at twice the frequency of the output motion of the actuator. This demonstrates that passing through the singularity does not degrade the natural frequency, and nearly doubles the actuator's displacement by allowing the input PZT stacks to cycle twice as fast.

The free displacement of a single PZT stack run at the test voltage is only 37 μm, where as the peak-to-peak displacement of the developed actuator has reached 2.37 mm. Therefore, the effective amplification ratio is over 64. This displacement amplitude was achieved at a frequency of 26.5 Hz. The input voltages to the PZT stacks were identical square waves at 53 Hz. Fig. 4-9 shows the input square wave signal and output displacement as functions of time.

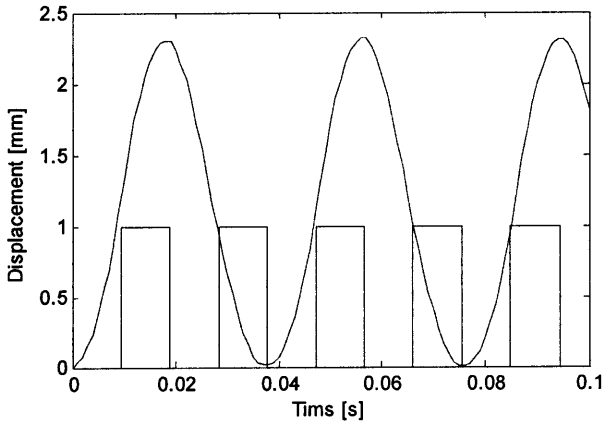

Figure 4-9: Input square wave signal and output response for actuator dynamically passing through the singularity point.

This prototype was also used to validate the nonlinear force-displacement relationship shown in Fig. 4-10. The driving voltage used to obtain the force data corresponds to an unforced length change in the PZT stacks of 88% of the maximum free displacement. Therefore, the data is plotted along with the theoretical force dis-

placement relationship for a 0.88 activation level. The slight variations are most likely due to machining tolerances from production, and the limitations of approximating short flexures as beams.

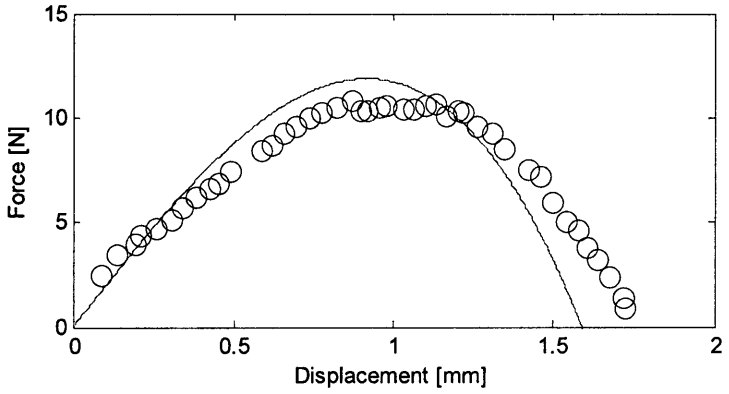

Figure 4-10: Theoretical and experimentally measured force-displacement data using an activation level of 88%.

4.6.2 Redirecting Stiffness Implementation

To demonstrate the degree of control granted by redirecting the principle axes of the stiffness matrix and using lateral activation, another proof-of-concept prototype was designed, built, and tested. The prototype performs exactly as it was designed to. With respect to the orientation in Fig. 4-11, when only the left PZT stack is actuated, the actuator output moves down, and when only the right PZT stack is actuated, the actuator output moves up. It is difficult to view in the figure because the ratio of x_s to y_s is approximately 50, but the orientation of the redirecting stiffness goes from lower left, to upper right. This validates the technique of using a redirecting stiffness in conjunction with lateral activation of the PZT stacks to control the direction of output displacement.

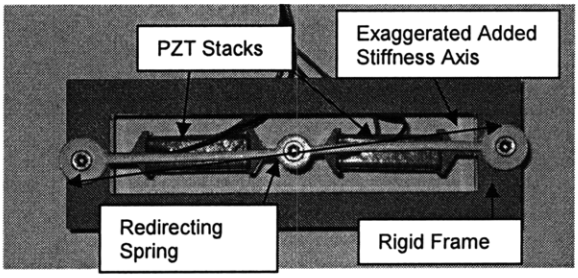

Figure 4-11: Displacement direction control prototype. The axis of the redirecting spring is exaggerated to emphasize that it is not parallel with the PZT Stacks.

Chapter 5

Multiple Buckling Units

5.1 Multiple Units Out of Phase to Control Buckling Direction

An alternative method to control the output displacement direction is to use multiple buckling actuators. Consider two buckling actuator units arranged in parallel, as shown in Fig. 5-1. We know that a single unit buckling actuator can essentially disengage from the system it is in when near the singularity point, so it is similarly possible to mechanically couple the output nodes of two units and have them interfere very little with each when each is near its singularity point. If the two units are in phase as in Fig. 5-1(a), then each unit is only disengaged when the other is as well. With this in-phase orientation, the actuator does not take advantage of a single unit's ability to disengage from the other. However, if the two units are out of phase as in Fig. 5-1(b), then when one unit is near its singularity point, the other is capable of producing much greater force. Thus, when one unit can effectively disengage, the other unit can still influence the output load.

If the inactive equilibrium angle, θ_0, (shown in Fig. 5-1(b)) is small enough then the bucking direction of the pair of units can be controlled. This is demonstrated in Fig. 5-2. At t_1, both units are inactive in both a) and b). Control is possible if activating one unit and not the other will force the inactive unit's output node through

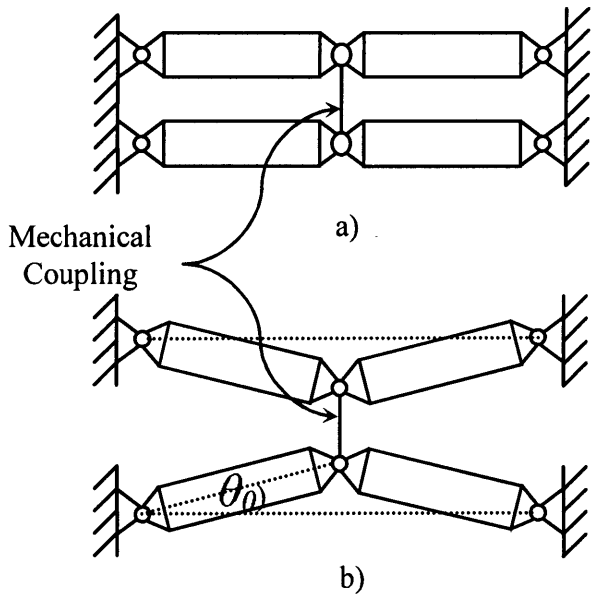

Figure 5-1: Diagrams of dual-unit buckling actuators a) spatially in phase, and b) spatially out of phase.

its singularity point. In Fig. 5-2, at time t_2, one unit is activated; the bottom unit for a) and the top unit for b). In both cases, the active unit has forced the inactive unit through its singularity position. Once the output nodes of both units are on the same side of their respective singularity points, activating both causes further displacement, as seen at time t_3 in Fig. 5-2. This requires the top and bottom pairs to be activated asynchronously, or temporally out of phase. Fig. 5-2 demonstrates that this phased activation can move the output nodes up or down. Thus the phased array actuator utilizes both being out of phase spatially and being activated out of phase temporally.

The advantages of using multiple out-of-phase units instead of redirecting the output node's stiffness are 1) no additional mechanical element is required to provide a redirecting stiffness, and 2) the output force can be more uniform over the range of displacement. The additional mechanical stiffness element used in the redirecting method inherently degrades performance by absorbing strain energy that would otherwise be applied to the output. The shape, and the uniformity of the force-displacement curve is dependent upon the initial displacements of the output nodes. There are two disadvantages of using multiple out-of-phase units to note. The first

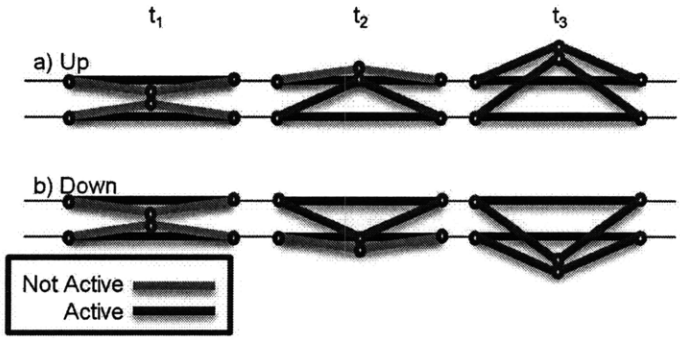

Figure 5-2: Asynchronous activation time sequence of dual-unit phase-shifted buckling actuator showing a) upward free displacement, and b) downward free displacement.

is that some strain energy will always be stored the two units because of each unit's conflicting unforced position. This strain energy is not applied to output. The second disadvantage is that tensile strain is required in the input actuators to return to the inactive unforced position, whereas, if used, the redirecting stiffness element provides the necessary restoring force. The tensile strain may pull apart the individual layers that make up PZT stack actuators and damage the input actuators if the strain is great enough in magnitude and no pre-loading mechanism for each individual stack is utilized.

5.2 Multi-Unit Out-of-Phase Actuator Simulation

As with the simulation for the single unit buckling actuator, the series stiffnesses of the piezoelectric actuators and compressive stiffness of the joints were modeled as springs, while the activation levels of the piezoelectric actuators were modeled as effectively changing the rest length of those springs. For the multi-unit out-of-phase actuator simulation, I used PZT stacks with length, L, of 40 mm, a maximum free displacement, u_{max}, of 42 μm, and stack stiffness of 800 N/42 μm = 1.9e8 N/m [14]. These values match the values of the PZT actuators used in the implementation of the concept. The rotational joints are modeled as flexures with certain axial and bending compliances determined by material and specified geometry. The flexure material is modeled as steel with a Young's modulus of 200 GPa. The potential energy, U, is a

function of displacement, y, and the top PZT stack pair and bottom PZT stack pair unforced length variation levels, u_t and u_b respectively. The total potential energy, U, is given by,

$$U = 2\left(\tfrac{1}{2}k_a\left((\Delta L_t)^2 + (\Delta L_b)^2\right)\right) + 4\left(\tfrac{1}{2}k_r\left((\Delta\theta_t)^2 + (\Delta\theta_b)^2\right)\right), \tag{5.1}$$

where k_a is the axial stiffness between an output node and grounded node accounting for flexure and PZT stack stiffness, k_r is the bending stiffness of each flexure, ΔL_t is the actual change in length from the inactive, unforced length between the top output node and either top grounding point, ΔL_b is the actual change in length from the inactive, unforced length between the bottom output node and either bottom grounding point, θ_t is the magnitude of the change in angle from the rest angle of either top PZT stack, and θ_b is the magnitude of the change in angle from the rest angle of either bottom PZT stack. ΔL_t, ΔL_b, $\Delta\theta_t$, and $\Delta\theta_b$ are calculated as,

$$\begin{aligned}
\Delta L_t &= \sqrt{(L\cos\theta_0)^2 + (y - L\sin\theta_0)^2} - (L + u_t), \\
\Delta L_b &= \sqrt{(L\cos\theta_0)^2 + (y - L\sin\theta_0)^2} - (L + u_b), \\
\Delta\theta_t &= \arctan\left(\tfrac{L\sin\theta_0 - y}{L\cos\theta_0}\right), \\
\Delta\theta_b &= \arctan\left(\tfrac{L\sin\theta_0 + y}{L\cos\theta_0}\right),
\end{aligned} \tag{5.2}$$

where L is the inactive, unforced length between either output node and either of its respective grounded points, and θ_0 is the inactive, unforced magnitude of the angle a PZT stack makes with the axis perpendicular to the output axis. θ_0 is geometrically related to the rest initial displacement of the output nodes.

The potential energy values for three activation scenarios are shown in Fig. 5-3. The graphs show the potential energy with two different values of the rest angle, θ_0; 0.3 degrees and 1.0 degrees. When both units are inactive, as in Fig. 5-3(a) there is a single potential energy well at zero displacement. Regardless of the output position, there is a restoring force to the zero displacement position. This means that even if the output node of one of the units was extended beyond its singularity point, the actuator would still provide a restoring force. This is true regardless of the rest angel,

θ_0.

When a single unit is active, as in Fig. 5-3(b), there is a nonzero slope in the potential energy function at a displacement value of zero. This means that at the rest position, the output nodes will be forced in one direction. Notice that in Fig. 5-3(b) for $\theta_0 = 1.0$ degrees, there is only one energy well, indicating that there exists just one unforced stable position. This is because this particular configuration simulated was designed such that there would always be force toward a preferred side of the rest position. However, it is possible to have a design that would generate two energy wells, one on either side of the rest position, if the rest angle, θ_0, is smaller. This is the case in Fig. 5-3(b) for $\theta_0 = 0.3$ degrees. Although, even with two equilibrium positions, the slope of the energy curve at the rest position is still nonzero, and the output would be forced in a preferred direction if it were at the rest position. By using a design with just one energy well, more control over the output is achieved, but at the cost of efficiency because a greater amount of energy from the input actuators is converted to strain energy within the actuator when both are activated as seen in Fig. 5-3(c).

When both units are active, two symmetric unforced equilibrium points exist. These equilibrium displacements are greater in magnitude than the equilibrium point of greatest magnitude (whether 1 or 2) from activating just one unit. Also the maximum force is greater with both units active than with just one unit active. This can be seen by observing that the maximum negative mid-stroke slope in Fig. 5-3(c) is greater than the maximum negative mid-stroke slope of Fig. 5-3(b). Thus, the simulation shows that activating one unit, followed by the other after the output is beyond the zero displacement point, is a method of controlling the buckling direction of the actuator.

5.3 Multi-Unit Phase-Shifted Implementation

To demonstrate the degree of control granted by including two buckling units and using asynchronous activation, a multi-unit phase-shifted prototype was designed,

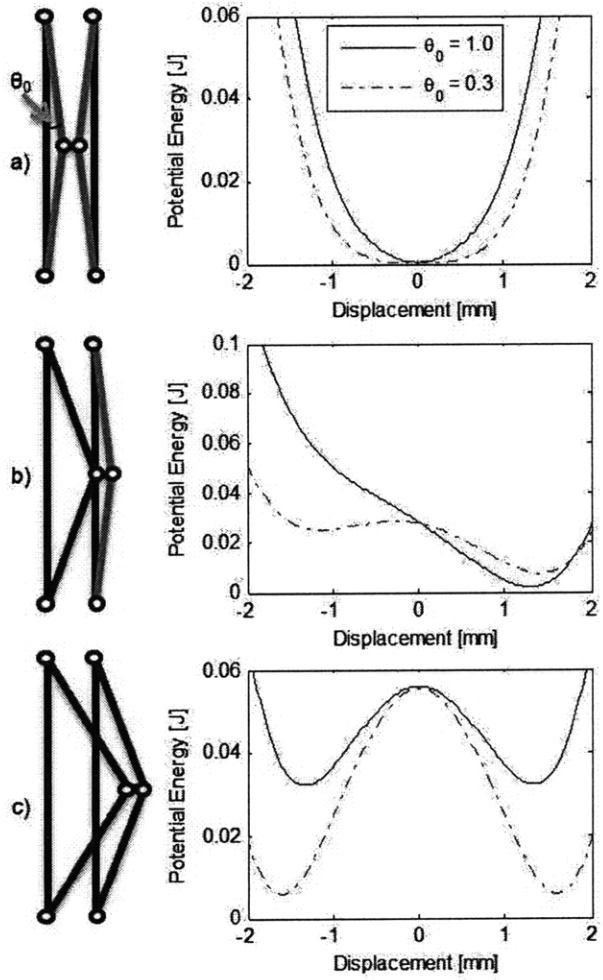

Figure 5-3: Potential energy vs. displacement simulation plots of dual-unit out-of-phase actuator when a) neutral, b) left unit active, and c) both units active.

built, and tested. It is shown if Fig. 5-4.

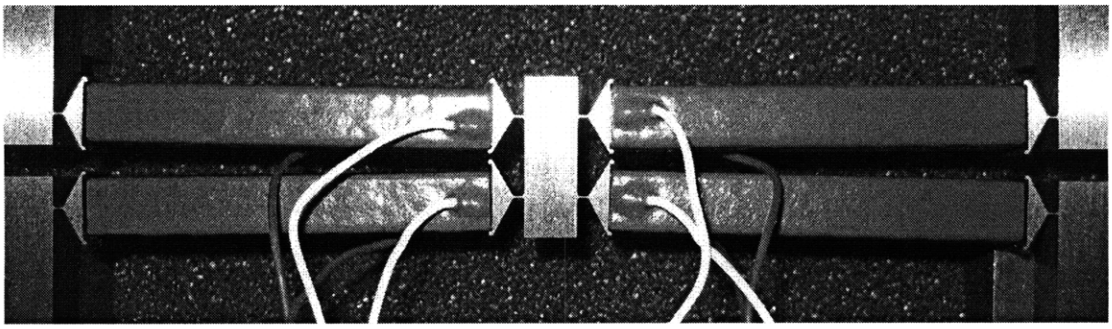

Figure 5-4: Multi-unit phase-shifted prototype.

The graph of the output displacement in Fig. 5-5 shows the performance when using asynchronous activation with zero load. First the bottom unit is activated generating greater than 1 mm of displacement, followed by the top unit generating a total of about 2.5 mm of displacement. The top unit then is deactivated, followed by the bottom unit. Then the order of activation is reversed and repeats generating similar displacements. The multi-unit phase-shifted actuator consistently generates 4.9 mm of peak-to-peak free displacement. This design was specified to generate just one equilibrium position when one unit is active, as with $\theta_0 = 1.0$ in Fig. 5-3, to give a large degree of control. If the rest angle, θ_0, were to be decreased, output performance would increase but at the expense of robust directional control.

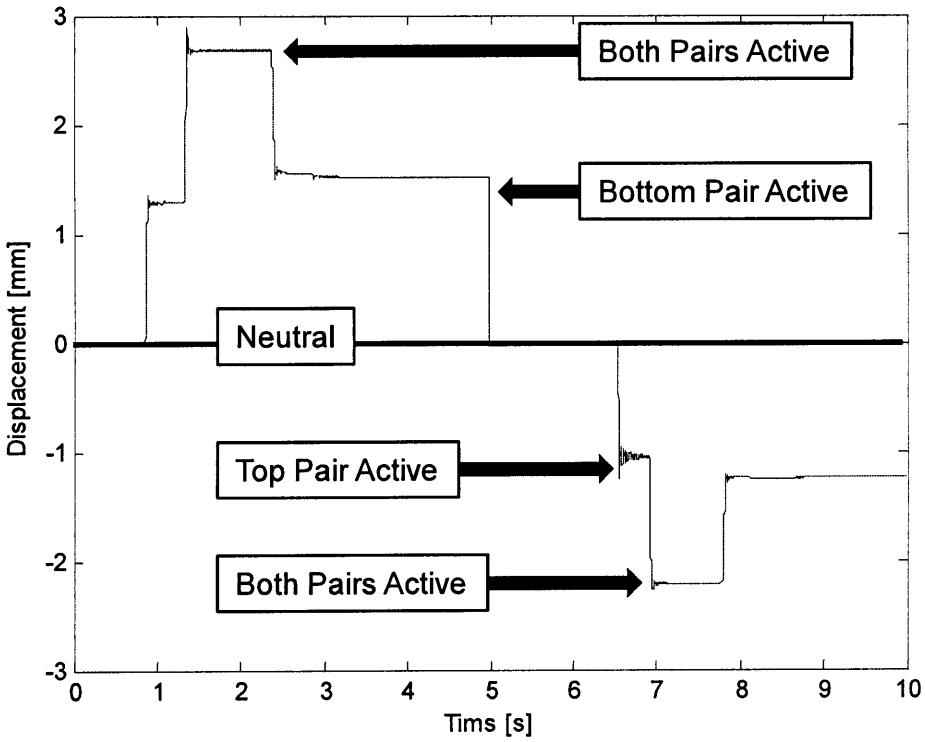

Figure 5-5: Output free displacement performance of multi-unit phase shifted prototype.

Chapter 6

Conclusion

This thesis has presented two significant displacement amplification designs. One is similar to tradition rhombus shaped actuators and is intended to be incorporated into multi-layer piezoelectric actuators. The preliminary kinematic analysis has shown that an array of output force-displacement characteristics can be selected for by the designer. These range from a negative sloped linear curve, to a relatively constant force curve, to a bistable negative parabolic curve. Initial prototypes and kinematic analysis have been used to identify numerous design considerations, including input actuator shear force and the critical compression angle, θ_c. A metric for output performance, energy per stroke by volume, has been presented and static mechanics and kinematic relations have been shown to be capable of optimally designing the mechanism to maximize this metric. A single layer actuator has been designed, built, and tested that amplifies strain by a factor of 16.5 (0.083% to 1.37%) while only reducing output force by a factor of 6.36 (800 N to 126 N). A preliminary second layer prototype has demonstrated that substantial second layer force is possible (19.9 N), though manufacturing limitations and scaling effects may limit output displacement.

The second design is the buckling actuator with two methods of controlling buckling direction using asynchronous activation. Large displacement is crucial for PZT actuated mechanisms to be useful for a broad range of robotic applications. Likewise, high force through a wide range of mid-stroke displacements, variable compliance, and the ability to effectively disengage are essential properties of actuators for specific de-

signs. The controlled buckling actuators presented show significant displacement with a single amplification phase, and controlled movement across a singular configuration. These actuators perform well statically and over a wide range of frequencies. The results presented suggest that the buckling actuator is well suited to many specific design criteria in the field of robotics. Future work includes utilizing multiple buckling actuators in a modular system, and utilizing them in locomotion applications.

Bibliography

[1] J. E. Huber, N. A. Fleck, and M. F. Ashby, "The selection of mechanical actuators based on performance indices," *Proceedings: Mathematical, Physical and Engineering Sciences*, vol. 453, no. 1965, pp. 2185–2205, 1997.

[2] L. Bay, K. West, P. Sommer-Larsen, S. Skaarup, and M. Benslimane, "A conducting polymer artificial muscle with 12% linear strain," *Advanced Materials*, vol. 15, no. 4, pp. 310–313, 2003.

[3] R. Pelrine, R. Kornbluh, Q. Pei, and J. Joseph, "High-speed electrically actuated elastomers with strain greater than 100%," *Science*, vol. 287, no. 5454, p. 836, 2000.

[4] N. Conway, Z. Traina, and S. Kim, "A strain amplifying piezoelectric MEMS actuator," *Journal of Micromechanics and Microengineering*, vol. 17, no. 4, pp. 781–787, 2007.

[5] C. Niezrecki, D. Brei, S. Balakrishnan, and A. Moskalik, "Piezoelectric actuation: state of the art," *The shock and vibration digest*, vol. 33, no. 4, pp. 269–280, 2001.

[6] W. Toulis, "Flexural-extensional electromechanical transducer," 1966. US Patent 3,277,433.

[7] R. Newnham, A. Dogan, Q. Xu, K. Onitsuka, J. Tressler, and S. Yoshikawa, "Flextensional moonie actuators," in *IEEE 1993 Ultrasonics Symposium, 1993. Proceedings.*, pp. 509–513.

[8] A. Dogan, K. Uchino, and R. Newnham, "Composite piezoelectric transducer with truncated conical endcaps Cymbal," *IEEE Transactions on Ultrasonics, Ferroelectrics and Frequency Control*, vol. 44, no. 3, pp. 597–605, 1997.

[9] K. Onitsuka, A. Dogan, J. Tressler, Q. Xu, S. Yoshikawa, and R. Newnham, "Metal-Ceramic Composite Transducer, the" Moonie"," *Journal of Intelligent Material Systems and Structures*, vol. 6, no. 4, p. 447, 1995.

[10] J. Ueda, T. Secord, and H. Asada, "Static lumped parameter model for nested PZT cellular actuators with exponential strain amplification mechanisms," in *IEEE International Conference on Robotics and Automation, 2008. ICRA 2008*, pp. 3582–3587, 2008.

[11] R. Van der Linde, "Active leg compliance for passive walking," in *1998 IEEE International Conference on Robotics and Automation, 1998. Proceedings*, vol. 3, 1998.

[12] S. Avadhanula, R. Wood, D. Campolo, and R. Fearing, "Dynamically tuned design of the MFI thorax," in *IEEE International Conference on Robotics and Automation, 2002. Proceedings. ICRA '02*, vol. 1, 2002.

[13] L. Howell, *Compliant mechanisms.* Wiley-Interscience, 2001.

[14] Thorlabs.com, "Piezo-electric actuators," August 2009. www.thorlabs.com.